ELSEVIER

Journal of Power Sources 55 (1995) 167–176

JOURNAL OF POWER SOURCES

Thermal relaxation during dynamic fuel cell operation

S. Hauff, K. Bolwin *

German Aerospace Research Establishment (DLR), Institute for Technical Thermodynamics, Pfaffenwaldring 38–40, 70569 Stuttgart, Germany

Received 6 September 1994; in revised form 20 December 1994; accepted 24 December 1994

Abstract

Energy conversion in electrochemical power devices is increasingly correlated with high density waste heat generation, since cell stacks have become highly compact. To predict the transient thermal behaviour of fuel cells, a three-dimensional simulation of their stack operation has been developed. Time constants of the transient response following load changes are determined and are in good agreement with experimental data obtained from a 100 W fuel cell stack.

Keywords: Fuel cells; Thermal conductivity

1. Introduction

In recent years, the improvement of fuel cell power density was a development goal of high priority. However, an essential problem of high density power devices is the rejection of a considerable amount of waste heat from a small volume. Thus, understanding the thermal behaviour of fuel cells during stationary and transient operation receives increasing attention. In particular, knowledge about the temperature distribution within the fuel cell stack is required to avoid thermal damage during its operation. However, there is little experimental data available, since probes cannot be integrated into the compact electrode stack. Thus, simulation of the stacks' thermal behaviour is essential to gain a better understanding of heat generation and dissipation processes.

The present investigation is an extension of our recent work [1] on a simple one-dimensional model to predict spatial- and time-dependent temperature profiles in alkaline fuel cells designed in the VARTA Eloflux concept [2–5].

The simulation presented in Ref. [1] is based on rough simplifications since thermal conductivity is restricted to the direction perpendicular to the electrodes and no spatial temperature distribution has been assumed across the electrodes. Nevertheless, these simple calculations succeed in predicting the temperature versus load characteristics of an equilibrium state fuel cell operation and give a rough estimate of time constants for thermal relaxation after load changes. However, the one-dimensional model failed to describe the detailed time-dependent temperature profiles during dynamic fuel cell operation.

2. Theory

Considering a certain volume element of the fuel cell, heat transfer across its boundaries and its own heat generation will cause changing temperatures and thus a variation of the internal energy of the volume element. The time dependence of the internal energy can be expressed by:

$$\frac{\partial u}{\partial t} = c_p \rho \frac{\partial T}{\partial t} \tag{1}$$

where ρ and c_p denote mass density and the heat capacity, respectively; ∂u describes the internal energy of the volume element unfolded by dx, dy and dz.

The temperature of this volume changes due to the thermal flux across its boundaries. Since the heat conductivity λ generally is assumed to be anisotropic, the partial derivation of the spatial temperature distribution is given by three differential equations for the three dimensions, respectively:

$$\dot{q}_x = -\lambda_x \frac{\partial T}{\partial x} \tag{2a}$$

* Corresponding author.

SSDI 0378-7753(95)02179-K

$$\dot{q}_y = -\lambda_y \frac{\partial T}{\partial y} \tag{2b}$$

$$\dot{q}_z = -\lambda_z \frac{\partial T}{\partial z} \tag{2c}$$

where the $\dot{q}_i$ ($i=x, y, z$) denotes the thermal fluxes. Striking the thermal balance of this volume element, including the heat q_E generated inside, leads to the continuity equation in its differentiated form:

$$c_p\rho \frac{\partial T}{\partial t} - \frac{\partial}{\partial x}\left(\lambda_x \frac{\partial T}{\partial x}\right) - \frac{\partial}{\partial y}\left(\lambda_y \frac{\partial T}{\partial y}\right) - \frac{\partial}{\partial z}\left(\lambda_z \frac{\partial T}{\partial z}\right) + \dot{q}_E = 0 \tag{3}$$

Considering those volume elements that are run through by the coolant flow, the enthalpy flux within the coolant contributes to the thermal balance. Thus, the last term of Eq. (3) must be extended by the thermal flux $\dot{q}_F = (m_F c_{p,F} \Delta T_F)/(\mathrm{d}x\ \mathrm{d}y\ \mathrm{d}z)$ that is carried within the coolant flow. Neglecting the temperature dependence of the heat conductivity λ simplifies Eq. (3) and results in an inhomogeneous, linear partial differential equation of the second order that is known as a Fourier differential equation:

$$\frac{\partial T}{\partial t} = \frac{1}{c_p\rho}\left(\lambda_x \frac{\partial^2 T}{\partial x^2} + \lambda_y \frac{\partial^2 T}{\partial y^2} + \lambda_z \frac{\partial^2 T}{\partial z^2} + \dot{q}_E\right) = a_{x,y,z} \nabla^2 T + \frac{\dot{q}_E}{c_p\rho} \tag{4}$$

where the a_i, defined as $a_i = \lambda_i/c_p\rho$ ($i=x, y, z$), reflects the anisotropy of the thermal conductivity.

Since the fuel cell is composed of various layers of different materials, an analytical solution of Eq. (4) cannot be given. Thus, a numerical formulation of this problem is required. As an approach to the exact solution, the continuous temperature distribution is replaced by a discrete network of temperatures.

A detailed description of the difference method applied to solve Eq. (4) is given in Ref. [6] for the one-dimensional case. This method is particularly suitable for describing heat-conduction phenomena across multiple layers of different materials.

In this discrete notation Eq. (4) can be written as:

$$\frac{\Delta_{x,y,z} T}{\Delta t} = a_x \frac{(\Delta_t^2 T)_{y,z}}{\Delta x^2} + a_y \frac{(\Delta_t^2 T)_{x,z}}{\Delta y^2} + a_z \frac{(\Delta_t^2 T)_{x,y}}{\Delta z^2} + \frac{\dot{q}_E + \dot{q}_F}{c_p\rho} \tag{5}$$

In order to determine a certain temperature $T_{l,m,n,k}$ in a four-dimensional parameter array, the temperature differences in Eq. (5) are expressed by the array elements. Here, indices l, m, n and k refer to the position vector $\vec{r} - \vec{r}_0 = (x_l, y_m, z_n) = (l\Delta x, m\Delta y, n\Delta z)$, and to the time $t_k - t_0 = k\ \Delta t$, respectively.

$$(\Delta_t^2 T)_{y,z} = T_{l+1,m,n,k} + T_{l-1,m,n,k} - 2T_{l,m,n,k} \tag{6a}$$

$$(\Delta_t^2 T)_{x,z} = T_{l,m+1,n,k} + T_{l,m-1,n,k} - 2T_{l,m,n,k} \tag{6b}$$

$$(\Delta_t^2 T)_{x,y} = T_{l,m,n+1,k} + T_{l,m,n-1,k} - 2T_{l,m,n,k} \tag{6c}$$

$$\Delta_{x,y,z}^2 T = T_{l,m,n,k+1} - T_{l,m,n,k} \tag{6d}$$

Starting from a well-known temperature distribution as assumed for $t=t_k$ we can calculate the temperature distribution for $t=t_{k+1}=t_k+\Delta t$. In a three-dimensional Cartesian matrix, unfolded by the parameters l, m and n, the transient temperature distribution can be calculated by the following approximation:

$$\begin{aligned} T_{l,m,n,k+1} = T_{l,m,n,k} &+ \frac{a_x \Delta t}{(\Delta x)^2} \times (T_{l+1,m,n,k} + T_{l-1,m,n,k} - 2T_{l,m,n,k}) \\ &+ \frac{a_y \Delta t}{(\Delta y)^2} (T_{l,m+1,n,k} + T_{l,m-1,n,k} - 2T_{l,m,n,k}) \\ &+ \frac{a_z \Delta t}{(\Delta z)^2} (T_{l,m,n+1,k} + T_{l,m,n-1,k} - 2T_{l,m,n,k}) \\ &+ \frac{\dot{q}_E + \dot{q}_F}{c_p\rho} \Delta t \end{aligned} \tag{7}$$

This formulation of the heat-conduction problem implies the simplification that the balance of the energy flows as expressed in Eq. (3) will not change during Δt. However, the thermal balance changes continuously and causes stability problems in the numerical calculations. The finite spacing of the matrix elements (Δx, Δy, Δz, Δt) are crucial for the effort, precision and stability of the difference method. In particular, increasing Δt will cause thermal flows higher than needed to even out the temperature differences between neighbouring volume elements and subsequently change the sign of the temperature gradient. This will cause an instability in the difference method applied.

These oscillations can be avoided by introducing a stability criterion to determine an upper limit for the time interval Δt, depending on the width of the spatial intervals Δx, Δy and Δz. For one dimensional heat conduction this stability criterion is defined assuming the Binder–Schmidt method [7] by: $p = a\Delta t/(\Delta x)^2$. The value of p can be simply estimated assuming steady-temperature distribution, and $T_{l,k}$ differs from this temperature level only. The restriction to one dimension allows a temperature balancing over three neighbouring volumes $l-1$, l, and $l+1$ only. Considering the limiting conditions of our assumption and neglecting heat sources and sinks leads to a one-dimensional expression of Eq. (7):

$$\Delta T_{l,\Delta k} \leqslant 2p\Delta T_{\Delta l,k} \tag{8}$$

where $\Delta T_{l,\Delta k}=T_{l,k+1}-T_{l,k}$ and $\Delta T_{\Delta l,k}=T_{l\pm1,k}-T_{l,k}$ denote the temporal and spatial temperature differences, respectively. Since the temporal temperature changes of volume l must not exceed the spatial temperature differences to its neighbours, $\Delta T_{l,\Delta k}<\Delta T_{\Delta l,k}$, and the stability criterion can be estimated to:

$$p_x \leqslant 1/2 \tag{9}$$

in its extension to three dimensions Eq. (9a) is written as:

$$p_x+p_y+p_z \leqslant 1/2 \tag{9b}$$

From this we derive an upper limit for Δt to avoid oscillations during the numerical calculation:

$$\Delta t \leqslant \frac{1}{2}\left(\frac{a_x}{\Delta x^2}+\frac{a_y}{\Delta y^2}+\frac{a_z}{\Delta z^2}\right)^{-1} \tag{10}$$

Since this stability condition must be fulfilled, that layer which leads to the lowest Δt determines the spacing of the grid. Although this model reflects the real condition, it is not practicable since: (i) the number of volume elements is limited by the capacity of the computer, and (ii) the time required for calculation increases by a power of four as the grid spacing decreases.

In order to obtain moderate computing conditions with a highest reliability of the results, heat conduction parallel to the electrode surfaces ($x-y$-plane) is treated different from that perpendicular to the electrodes (z-direction). For the z-direction, that predominates the overall thermal balancing, the spacing of Δt is determined according to Eq. (10). Thermal balancing in the $x-y$ plane is considered subsequently to the heat conduction directed parallel to its normal vector. To contribute to tolerable computing requirements, only a rough spacing of Δx and Δy is considered. This coarse spacing within the structural elements causes a re-alignment of the heat conductivity λ_x and λ_y and thus a re-alignment of the factors a_x and a_y:

$$a_x=\frac{\Delta x^2}{\Delta t}p_z \tag{11a}$$

$$a_y=\frac{\Delta y^2}{\Delta t}p_z \tag{11b}$$

Note that this simplification will not affect the heat conduction from the source to the sink, since they are located in different structural elements.

In the present simulation, we consider different contributions to waste-heat generation, dissipation and rejection:

- reversible and irreversible heat generation during the electrochemical reaction: entropy changes; polarization losses, and ohmic losses within the electrolyte
- Joulean heat generation within the electrodes
- heat transition from the structural elements to the electrolyte (coolant) flow
- free convection at the fuel cell's surfaces

The waste heat generated during fuel cell operation has sufficiently been discussed in the past [5,8,9]. Its amount is mainly determined by the entropy changes and load-dependent overpotentials. Thus, the heat generated can be given by Eq. (12) as a function of applied current density and temperature at the reaction site:

$$\begin{aligned}\dot{Q}(i_{fc},T) &= \Delta H - zFu_{fc}(i_{fc},T)\\ &= \Delta H - zF[U^*-r_0 i_{fc}\exp(E_a/RT)]\end{aligned} \tag{12}$$

where $\dot{Q}$, u_{fc}, i_{fc} and T denote the waste-heat generation rate, the fuel cell's voltage, current density, and temperature, respectively. The parameters U^*, r_0 and E_a denote the open-loop voltage, the ohmic resistance and the activation energy of the fuel cell system under consideration. These parameters depend on individual cell configuration and geometry and can be derived experimentally.

The finite ohmic resistance within the conducting grid of the electrodes leads to a potential drop across the electrode and thus to local potentials $u_{fc}=u_{fc}(x,y)$ and current densities $i_{fc}=i_{fc}(x,y)$. The spatial potential distribution can be calculated according Kirchhoff's law. This potential distribution leads to inhomogeneous heat generation and thus to an inhomogeneous temperature profile across the electrodes' surfaces. This inhomogeneity of the temperature feeds back onto the waste-heat production rate via the temperature dependence of the fuel cell's characteristic (see Eq. (12)). Since the ohmic resistance is generally temperature dependent, the feedback of the temperature distribution on to the local potential must be considered.

In addition, Joulean heat generation within the electrodes contributes to the inhomogeneity of the temperature profile due to the anisotropic current-collection geometry.

Heat transition from the structural materials to the coolant flow and ambience has been considered accordingly to the appropriate Nusselt relations:

$$Nu=f(Re,Pr)=\frac{a}{\lambda}d \tag{13a}$$

and

$$Nu=f(Gr,Pr)=\frac{a}{\lambda}d \tag{13b}$$

for the heat transition to the coolant drain and for free convection, respectively. Here Re, Pr and Gr denote the Reynolds, Prandel and Grashof numbers, respectively. A detailed description of the Nusselt relations was recently given in Refs. [1,10].

3. Experimental

Experiments were carried out in order to obtain the characteristic parameters of the fuel cell stack considered as reflected in Eq. (12). On the other hand, the simulation has to be verified by experimental data. For this, the fuel cell stack has been modified during production to enable the measurement of distinct temperatures from inside the stack. The fuel cell consists of several layers performing different tasks:

- the electrodes serve for the electronic conduction and the chemical reactions taking place on their surfaces
- the separators insulate the electrodes from each other and are filled with an electrolyte to enable ionic conduction
- the so-called 'labyrinth layer' serves as a feed through for electrolyte and coolant flows

Due to the compact arrangement of the stack layers (e.g., electrodes and separators) it is not possible to place temperature probes on the electrodes and simultaneously ensure safe fuel cell operation. Thus, experimental temperature profiles are not obtainable from the electrodes.

The peripheral experimental setup serves the coolant/electrolyte management and the reactant supply of the fuel cell. The electrolyte circuit consists of an expansion tank containing the temperature control, a pump to revolve the electrolyte, and the casing. The product water is removed by evaporation and subsequent condensation on cooling traps of a secondary coolant circuit. The expansion tank simultaneously serves as evaporating tray for this water removal process.

The reactant-gas supply contains a humidification device to avoid damaging of the fuel cell by drying out their electrodes. Inert gases that accumulate during operation within the fuel cell can be removed by purging.

Considering further physical dimensions contributing to the thermal management of the fuel cell, the experimental setup was equipped with pressure gauges and flow meter for both electrolyte and reactant gases. In addition, the cell voltages and the current generation were monitored. The operating conditions of the fuel cell were adjusted by an electronic load.

The temperatures were recorded using NiCr–Ni thermocouples. Eight thermocouples were placed in each labyrinth layer, as indicated in Fig. 1. The channels shown in the Figure serve the electrolyte/coolant feed. The experiments were carried out using a 100 W fuel cell stack which contains three labyrinth layers. Thus, 24 temperatures are experimentally available across the cell stack.

In order to determine the thermal response to load changes during fuel cell operation, time-dependent temperature profiles must be recorded. These measurements were performed by a computer via an AD converter and an IEEE interface. Since only one ADC was available, the data lines were multiplexed. Thus, the transient resolution is restricted to 15 s when recording all accessible data.

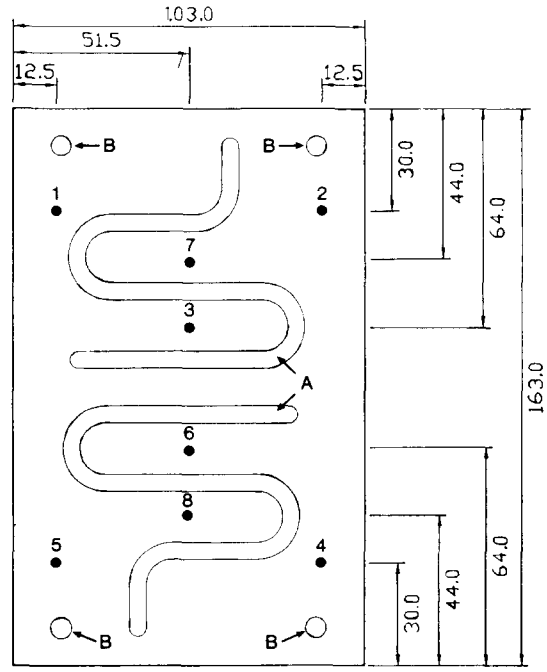

Fig. 1. Labyrinth layer of the Eloflux fuel cell with (A) coolant drains and (B) gas feedthroughs. The positions of the different thermocouples are indicated (1 to 8). All distances are given in mm.

4. Results and discussion

4.1. Determination of the characteristic fuel cell parameters

Consideration of the temperature-dependent waste-heat generation in thermal modelling of cell stacks requires an exact knowledge of the fuel cell's efficiency as a function of temperature and current density. Thus, the fuel cell's characteristic was experimentally determined for different temperatures ranging from ambient temperature to $T=60$ °C. These characteristics are shown in Fig. 2; they show almost linear behaviour except for low current. From these data, a fictive open-loop voltage of $U^*=1005$ mV is derived (see Fig. 2) which shows nearly no dependence on temperature. In accordance with Winsel [5], the nearly linear section of the temperature-dependent fuel cell characteristic can be approximated by:

$$u_{fc}=U^*-r_0 i_{fc}\exp(E_a/RT) \quad (14)$$

where r_0 denotes a resistance characteristic for the fuel cell system considered and E_a a characteristic activation energy.

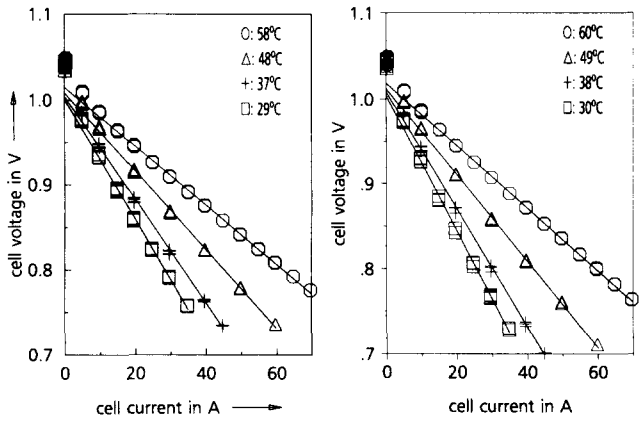

Fig. 2. Temperature-dependent fuel cell characteristics for two subsequent cell packages within a 100 W Eloflux cell stack.

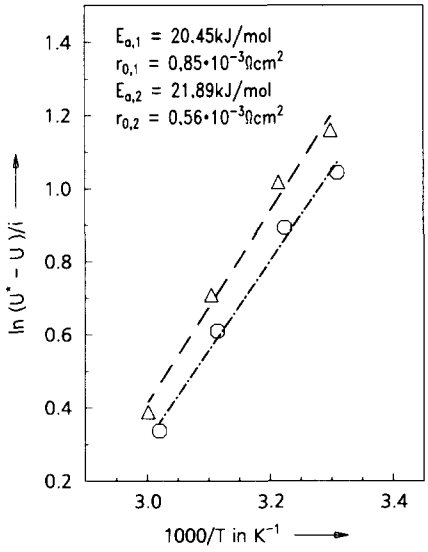

Fig. 3. Experimental determination of fuel cell properties as activation energy and internal resistivity by an Arrhenius's evaluation of the temperature-dependent characteristics.

The coefficients r_0 and E_a were determined applying an Arrhenius's evaluation. According to Eq. (15), the logarithm of the potential difference $\ln[(U^*-u(i))/i]$ is plotted against the inverse temperature, as shown in Fig. 3; a linear relationship should be found. Then the activation energy E_a and the specific resistance r_0 can be derived from the slope and the intercept, respectively:

$$\ln\left(\frac{(U^*-u_{fc})}{i_{fc}}\right)=\ln(r_0)+\frac{E_a}{R}\frac{1}{T} \quad (15)$$

For the fuel cell stack used in our experiments we found activation energies of $E_a=20.45$ kJ/mol and $E_a=21.89$ kJ/mol for the two cell packages, respectively. The internal specific resistance could be determined to $r_0=85$ mΩ cm^2 and $r_0=56$ mΩ cm^2. These results agree well with those reported in the literature for this type of fuel cell [5].

4.2. Equilibrium-state fuel cell temperature

Since the time constants of thermal relaxation are evaluated in terms of temperature differences with respect to the expected final-state equilibrium temperature (see Eq. (19)), the characteristic of equilibrium temperatures versus fuel cell load should be discussed prior to the consideration of the unsteady case. Secondly, the inhomogeneity of the spatial temperature distribution will limit fuel cell operation at higher operating temperatures. We give an attempt to evaluate the load dependence of the inhomogeneity in terms of fit parameters derived from the experimental or calculated temperature versus load characteristic.

The spatial distribution of equilibrium-state fuel cell temperatures has been calculated for different operating conditions of the cell stack. Fig. 4 shows the results of this calculation for selected positions within the cell stack. For comparability with experimental data, the temperatures presented are related to those volume elements corresponding to the thermocouple positions in the experiment. In Fig. 4, the positions within the cell stack are indicated by the indices of the corresponding thermocouples TC_{xy}. Here x and y refer to the labyrinth layer and to the position within the layer as given in Fig. 1.

The data are plotted against the current generation, which represents the fuel cell's load. Obviously, the equilibrium temperatures within the fuel cell stack do not depend linearly on the fuel cell load.

In order to find a quantitative expression for fuel cell temperature as a function of load, we plotted the logarithm of ΔT versus the logarithm of the current generation and found a linear relationship, as also shown in Fig. 4:

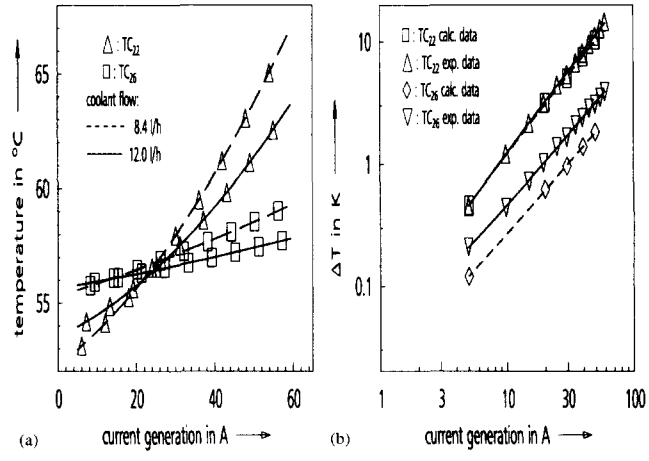

Fig. 4. Experimentally derived equilibrium temperatures vs. fuel cell load. The temperatures shown were measured with thermocouples nos. 2 and 6 in the second cell of the stack. (a) The temperatures were shown for different coolant flows. (b) Comparison with calculated data. The temperature differences refer to the equilibrium temperature at $I=0$ A, i.e., the electrolyte feed temperature.

$$\ln(\Delta T') = \ln a + b \ln I' \quad (16)$$

Here, ΔT denotes the difference between the equilibrium temperatures $T(I)$ and $T(I=0)$. The latter is mainly determined by the electrolyte-feed temperature. Note that $\Delta T'$ and $\Delta I'$ are nondimensional quantities (e.g. $I' = I/I_0$, $I_0 = 1$ A). Since coefficient b differs from unity, the temperature does not depend linearly on the current generation. This behaviour is observable in both the simulation results and the experimental data. The experimentally derived values for coefficient b vary from $1.02 \leqslant b \leqslant 1.55$. Note, that this formulation of the temperature versus load characteristic of the fuel cell is only a mathematical fit and is not based on physical principles. Thus, parameters a and b are not related to physical dimensions; however, they may be used to compare the model calculation with experimental results.

On the other hand, the coefficients from Eq. (16) can be used to discuss the behaviour of the temperature distribution as a function of fuel cell load. Increasing the current density, diverging temperatures at random but different positions within the fuel cell stack should result in a more inhomogeneous temperature distribution. Since the convergence behaviour of the temperature distribution can be expressed by the ratio of two temperatures rather than by their difference, the inhomogeneity of the temperature distribution can be expressed by:

$$f_{\text{conv}} = \frac{\Delta T_1'}{\Delta T_2'} = \frac{a_1}{a_2} I'^{(b_1 - b_2)} \quad (17)$$

where f_{conv}, denotes the convergence factor and indices 1 and 2 refer to different volume elements of the fuel cell stack. Convergence factors $f_{\text{conv}} < 1$ will lead to a more homogeneous temperature distribution, increasing the fuel cell load, whereas $f_{\text{conv}} > 1$ will increase the inhomogeneity of the temperature distribution.

From Eq. (17), the temperature ratios are obviously not affected by load variations for identical coefficients $b_i \equiv b_j$ of the data field. However, the experimental results indicate a variation of b_i depending on the position of the related volume element within the stack. Thus, we conclude, that the temperature ratios of the different volume elements i, j vary with increasing load. Depending on the coefficients a, b of the polynomial in Eq. (16), the temperature ratios and thus the inhomogeneity of the temperature distribution may increase or decrease with increasing load. However, if the fuel cell load is sufficiently high, the temperature ratios will diverge, since the polynomial with the higher exponent grows faster. These load limits can be estimated by determining the intersections of two random polynomials. Then, the limiting condition, that the fuel cell load must exceed a lower limit to show clearly a diverging temperature distribution, can be expressed for two sets of parameters a, b by a divergence criterion C_d defined as:

$$I' > C_d = \left(\frac{a_i}{a_j}\right)^{(1(b_j - b_i))} \quad (18)$$

Evaluating coefficients a_i and b_i, we found a wide variation of the defined divergence criterion. The frequency distribution of this divergence criterion $n(C_d)$ is shown in Fig. 5 by the dashed line. The integrated frequency distribution $N(C_d) = \int_{-\infty}^{C_d} n(c_d)\, dc_d$ as given by the solid line represents the probability that the divergence criterion (Eq. (18)) is fulfilled for random pairs of parameter sets.

Evaluating the statistical distribution of this divergence criterion we found that 75% of the possible parameter combinations fulfil this criterion in the load range of interest ($20\ \text{A} < I < 60\ \text{A}$). Thus we conclude that spatial temperature distribution will diverge with increasing fuel cell load.

Since the I versus U characteristic of the fuel cells depends on temperature, increasing inhomogeneity in the thermal distribution causes increasing inhomogeneity of the current density.

Although the equilibrium temperatures do not depend linearly on the load, the curvature of the T_{eq} versus I characteristic is small in the considered load range ($20\ \text{A} \leqslant I \leqslant 50\ \text{A}$) and only four data points are available from both dynamic simulation calculation and experiment. Due to the experimental error bars and the few data points, the evaluation of the coefficients from Eq. (16) is difficult and not suitable for comparing the system simulation with the experimental data.

However, as can be seen from Fig. 6, the T_{eq} versus I characteristic can almost be approximated by straight lines whose slope is related to the mean slope of the nonlinear expression of Eq. (16) by the relation

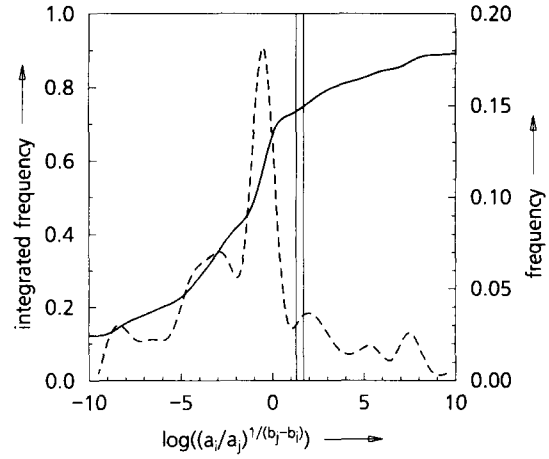

Fig. 5. Frequency distribution of the divergence criterion as defined in Eq. (18) (dashed line) and the integrated frequency distribution (solid line), which is interpreted as the probability of diverging temperature behaviour in the fuel cell stack.

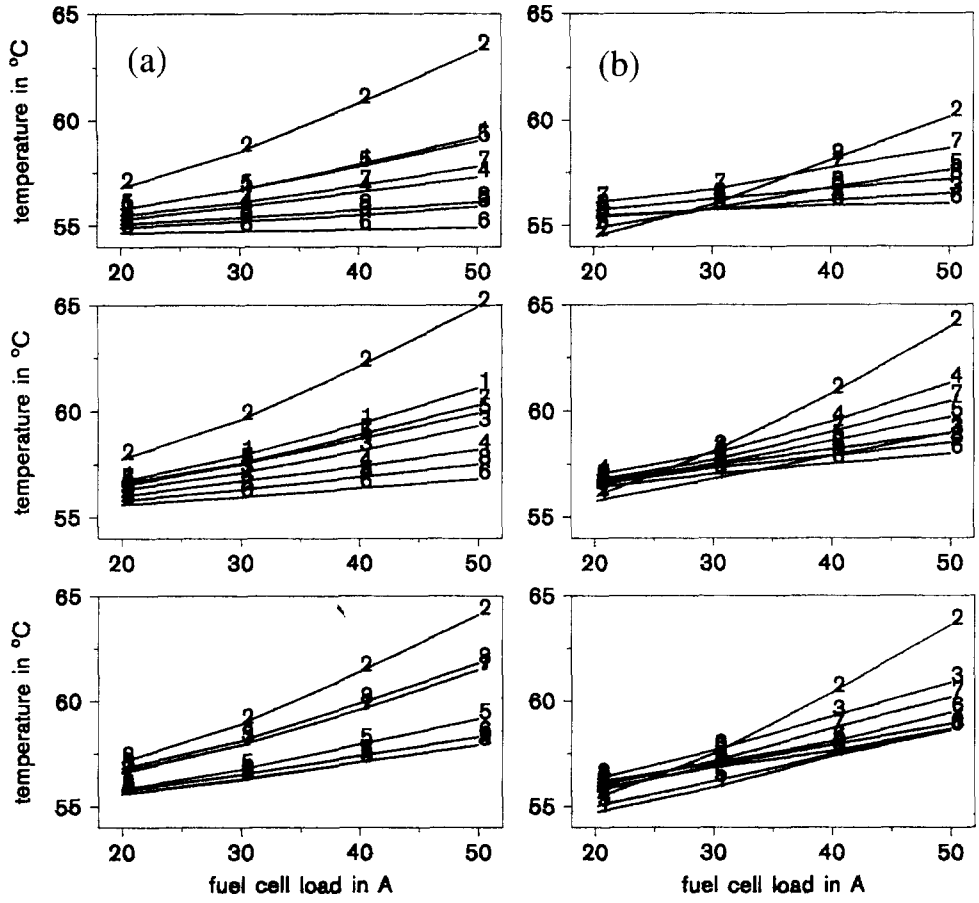

Fig. 6. Equilibrium temperatures vs. fuel cell load as derived from (a) calculated data and (b) from the experiment. The data are shown for the three labyrinth layers of the 100 W cell stack. The numbers refer to the thermocouple position as shown in Fig. 1.

$\Delta T/\Delta I = ab\hat{I}^{(b-1)}$. Here $\hat{I}$ denotes that current whose derivative equals the mean slope of the monotone function in a given range.

Fig. 7 gives a comparison of the crude linear approximation of the simulation data to the more detailed evaluation using Eq. (16). Assuming $\hat{I} = 35$ A, we found a good correlation between both evaluations as indicated by the parameters $m = 1.037$ and $a = -3.9 \times 10^{-3}$ K A^{-1} of the regression line. Thus, the mean slopes of the T_{eq} versus I characteristics are suitable for comparing the experiment and the system simulation. This comparison is shown in Fig. 8. Although the plotted data show a distinct scattering, the experimental data agree sufficiently with the system simulation results, as can be seen from the regression line parameters $m = 0.96$ and $a = 0.12$ K A^{-1}.

From this we conclude that the presented simulation program is suitable for giving a correct description of the dependence of equilibrium temperatures on fuel cell load.

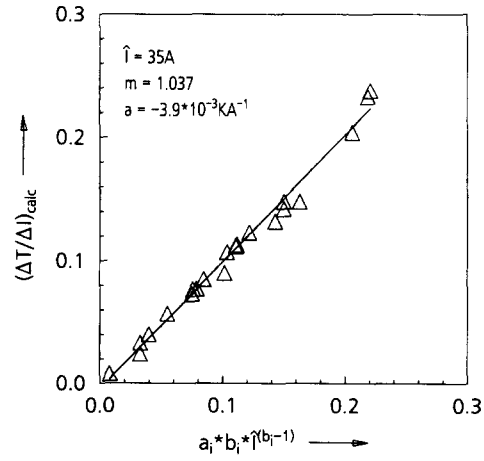

Fig. 7. Comparison of the crude linear evaluation of the T_{eq} vs. I characteristic from the system calculation, with the mean slope determined from coefficients a_i, b_i which were obtained from a more detailed nonlinear evaluation of calculated equilibrium temperatures.

4.3. Thermal response on load changes

The reason for performing dynamic calculations of heat and mass transport in fuel cells is to gain information on basic principles that drive the thermal relaxation of a fuel cell system after load changes. In addition, we given an attempt to relate the basic principles to the experimentally observable quantities. The

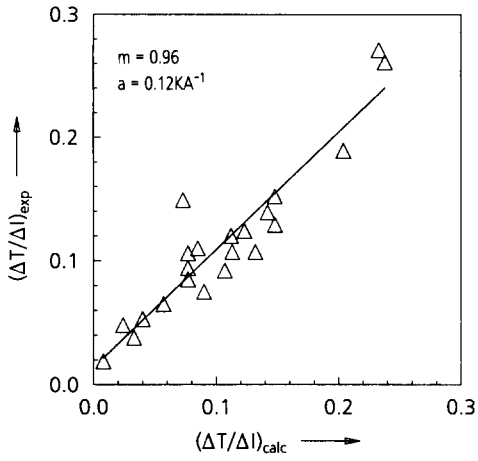

Fig. 8. Comparison of the experimental and calculated slopes of the T_{eq} vs. I characteristics.

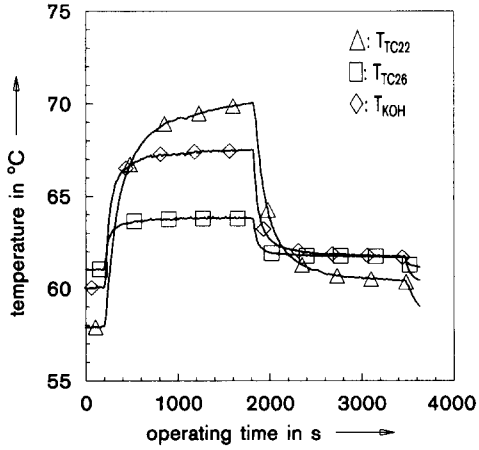

Fig. 9. Thermal relaxation of the fuel cell stack after load changes. The experimental data were measured with thermocouples nos. 2 and 6 in the second labyrinth layer. In addition, the temperature of the coolant (KOH) is shown.

basic principles of thermal relaxation are in general the heat fluxes and the heat transition, as discussed above in Section 2. Experimental observables of those processes are their time constants. Further, it is important to distinguish different contributions to the relaxation process and to identify the basic principles by which they are driven.

The thermal response of the fuel cell on load changes was measured starting from equilibrium-state fuel cell operation at $I=5$ A, corresponding to $i=12.5$ mA cm^{-2} and an electric power generation of $P_{el}=10$ W. Temperature data were recorded from the thermocouples in the labyrinth layer after increasing the electric load to $P_{el}=90$ W corresponding to $I=60$ A or $i=150$ mA cm^{-2}. Initially a steep increase of the temperature is observed, as shown in Fig. 9; however, the temperatures show asymptotic behaviour a few seconds later. Equilibrium temperatures have almost been achieved after a few hundred seconds. After the fuel cell has been operated for 1600 s at constant-current generation of $I=60$ A, the load was decreased to $I=20$ A, corresponding to $i=50$ mA cm^{-2} or $P_{el}=37.5$ W.

On the other hand, dynamic temperature calculations were performed for those volume elements that correspond with the positions of the thermocouples. The start parameters of this dynamic system modelling correspond with the initial conditions of the experimental setup. Running down the calculation, the load parameter was changed in order to simulate the experimental load profile of the fuel cell.

In this way, we generate two sets of transient temperature data, by experiment and system simulation. These data sets correspond to equal operating conditions of the fuel cell stack and are suitable for validating the system calculation.

In order to derive an analytical expression for the time dependence of the fuel cell temperatures, we suggest that the relaxation process after load changes can be qualitatively described in good approximation by an exponential behaviour. Then the transient coefficients describing the relaxation process can be evaluated by plotting temperature differences to the final-state equilibrium temperature $\Delta T=T_{eq,f}-T(t)$ in a logarithm scale versus time, as shown in Fig. 10.

It is clearly seen that the simple exponential description of the transient temperature behaviour failed, since the plot did not result in a linear relation of $\ln \Delta T$ and t. However, from Fig. 10 we conclude that the thermal relaxation can be described in general by a sum of different exponential terms:

$$T(t)=T_{eq,f}-\sum_{i=1}^{n}\alpha_i \exp(-\tau_i t) \tag{19}$$

where n denotes the number of terms, τ_i denotes the time constants, and the total difference between the initial- and final-state equilibrium temperatures is given by $\Sigma a_i=T_{eq,f}-T_{eq,i}$. Evaluating the data shows that only two terms ($n=2$) lead to a sufficiently good de-

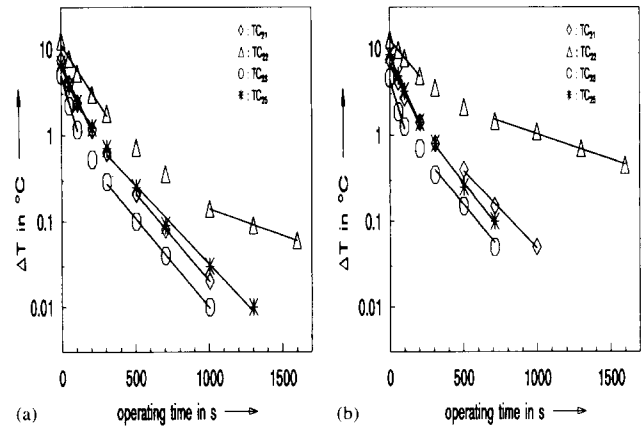

Fig. 10. Temperature differences with respect to the final equilibrium temperature: (a) calculated data and (b) experimental data.

scription of the thermal response on load changes. From this we conclude that two processes contribute to the thermal relaxation of fuel cells. The fast process shows transient constants in the range of 4.1×10^{-3} $s^{-1}<\tau_i<1.8\times10^{-2}$ s^{-1}, whereas the slower process shows transient constants ranging from $\tau_i<8.8\times10^{-4}$ s^{-1} to $\tau_i<6.8\times10^{-3}$ s^{-1}.

The suggestion that the fast process may be related to heat conduction perpendicular to the electrode surfaces (along the z-axis in the simulation model) and the slower process assigned to heat conduction within the structural components (e.g., electrode, separators), which corresponds to the x–y-plane, is based on the anisotropy of the heat conductivity. On the other hand, the relaxation process is very complex. Temperature changes affect the heat generation and cause a re-alignment of the current-density distribution. The slower process may reflect a re-alignment process occurring subsequently to the initial temperature changes. However, in our opinion, re-alignment processes run down quickly compared with the heat conduction within the cell stack. Secondly, the suggested anisotropic behaviour of the heat conduction is supported by the evidence of only one contribution to the thermal relaxation from a simple one-dimensional thermal simulation [1]. Thus the simple one-dimensional description of the transient temperature behaviour failed.

Temperature changes in a certain volume element are caused by heat fluxes across its boundary, as long as no heat sources or sinks are located in the volume element considered. Changes in the heat content of the volume elements can be expressed by the derivative of Eq. (19):

$$\dot{Q}=\rho c_p \frac{dT}{dt}\,dV$$

$$=-\rho c_p\,dV\sum_i \alpha_i\tau_i\exp(-\tau_i t)=\sum_i \dot{Q}_i \qquad (20)$$

On the other hand, these heat fluxes are driven by temperature gradients. Considering anisotropic heat conductivity (i.e., $\lambda=\lambda(\varphi,\vartheta)$) leads to the following expression of Eq. (4):

$$\frac{4}{3}\pi\rho c_p\frac{dT}{dt}=\int_0^{2\pi}\int_{-\pi}^{\pi}\lambda(\varphi,\vartheta)\frac{\partial^2 T(r,\varphi,\vartheta,t)}{\partial r^2}\,d\varphi\,d\vartheta \qquad (21)$$

Finally, from a comparison of Eqs. (20) and (21) and substitution of dT/dt in Eq. (21) by the appropriate expression from Eq. (20), we conclude that the experimentally identified contributions to the thermal relaxation of the fuel cell stack are related to anisotropic thermal conduction within the cell stack. Since we found evidence of only two contributions to the thermal relaxation, the anisotropy of the heat conduction is restricted to two nonequivalent directions. To account

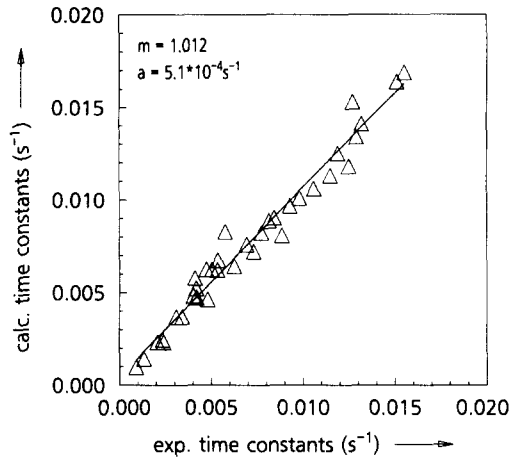

Fig. 11. Comparison of calculated and experimentally derived time constants describing the thermal relaxation of fuel cells during dynamic operation.

for two linear independent, nonequivalent directions, Eq. (21) should be expressed using cylindrical coordinates (z, r, φ). Then the empirically derived expression in Eq. (19) can be related to the heat conductivity by the following relation:

$$\sum_{i=1}^{2} a_i\tau_i\exp(-\tau_i t)=\frac{\lambda_z}{\rho c_p}\frac{\partial^2 T}{\partial z^2}+\frac{2\lambda_r}{\rho c_p}\frac{\partial^2 T}{\partial r^2} \qquad (22)$$

To validate the transient behaviour of the simulation model, the time constants from Eq. (19) have been evaluated for both calculated and experimental data. In Fig. 11, the calculated time constants are plotted against the experimental data. From a linear fit to these data, we derived a slope of $m=1.012$ and an intercept of $a=5.1\times10^{-4}$ s^{-1} for the regression line. Thus, a comparison of experimental and calculated time constants results in a functional relation that is very close to the identity operator. From this we conclude that the presented simulation model is suitable for giving a correct description of the time dependence of spatial temperature distributions with fuel cell stacks during dynamic operation.

5. Conclusions

A three-dimensional time-dependent simulation program has been developed in order to describe the temperature distribution within a fuel cell stack and its response to load changes.

The results of the model calculations have been verified by experimentally accessible temperatures obtained from measurements on an Eloflux fuel cell block. From the comparison of experimental and calculated temperatures we found a good agreement of the thermal modelling with the experiment concerning the differences of equilibrium temperatures related to different

operating states of the fuel cell. From the temperature versus load characteristic, we predict an increasing inhomogeneity of temperature distribution with increasing fuel cell load.

In addition, the transient behaviour of the experimental temperatures is described correctly by the simulation. We found two contributions to the thermal relaxation following the load changes during stack operation:

(i) a fast process showing transient constants $4.1\times 10^{-3}\ s^{-1}<\tau<1.8\times 10^{-2}\ s^{-1}$, and

(ii) a slower process with transient constants in the range $8.8\times 10^{-4}\ s^{-1}<\tau<6.8\times 10^{-3}\ s^{-1}$.

These thermal relaxation processes are related to the heat conduction perpendicular to the electrodes' surfaces and to in-plane heat conduction of the structural elements. Although the transient constants vary over more than one order of magnitude, we found a good correlation between experimental and calculated temperatures. Thus, the transient thermal behaviour of the fuel cell stack is correctly described by the simulation program.

6. List of symbols

$a_{x,y,z}$	thermal conductivity in x-, y- and z-directions ($m^2\ s^{-1}$)
c_d	divergence criterion
c_p	specific heat capacity (kJ $kg^{-1}\ K^{-1}$)
E_a	activation energy (kJ mol^{-1})
F	Faraday's constant (A s mol^{-1})
f_{conv}	convergence factor
Gr	Grashof number (−)
H	enthalpy (J mol^{-1})
I	current (A)
i_{fc}	current density of the fuel cell (mA cm^{-2})
m_F	mass flow of the coolant (kg s^{-1})
Nu	Nusselt number (−)
p, $p_{x,y,z}$	stability criterion (−)
Pr	Prandtl number (−)
q_E	heat generation rate (W m^{-2})
q_F	thermal flow within the coolant (W m^{-2})
$q_{x,y,z}$	thermal flow in x-, y- and z-directions (W m^{-2})
R	universal gas constant (J $mol^{-1}\ K^{-1}$)
r_0	internal area specific source resistance of the fuel cell ($\Omega\ cm^2$)
Re	Reynolds number (−)
t	time (s)
T	temperature (K)
T_{eq}	equilibrium temperature (K)
$T_{l,m,n,k}$	temperature of the volume element l, m, n at the time k (K)
u	internal energy (J)
u_{fc}	voltage of the fuel cell (V)
U^*	fictive open-loop voltage (V)
V	volume (m^3)

Greek letters

α	heat-transition coefficient (W $m^{-2}\ K^{-1}$)
$\lambda_{x,y,z}$	heat conductivity x-, y- and z-directions
ρ	density (kg m^{-3})
τ_i	time constant (s^{-1})

References

[1] A. Baumann, S. Hauff and K. Bolwin, *J. Power Sources, 36* (1991) 185–199.

[2] H. Holthusen, *Ph.D. Thesis*, Technical University of Braunschweig, 1972.

[3] A. Winsel and R. Wendtland, *DE Patent DBP No. 1 546 719* (1965).

[4] A. Winsel and R. Wendtland, *DE Patent DBP, No. 1 496 214* (1965).

[5] A. Winsel, *DECHEMA-Monogr., 92* (1982) 21–43.

[6] H. Schuh, *VDI-Forschungsh., 459* (1957).

[7] K. Stephan and F. Mayinger, *Thermodynamic Band 1, Grundlagen und technische Anwendungen, Einstoffsysteme,* Springer, Berlin, 1986.

[8] B.S. Baker, D. Gidaspow and D. Wasan, *Adv. Electrochem. Electrochem. Eng., 8* (1971) 63–156.

[9] A. Winsel, Galvanische Elemente, Brennstoffzellen, *Ullmanns Encyklopädie der technischen Chemie,* Vol. 12, Verlag Chemie, Weinheim, Germany, 1982, pp. 113–136.

[10] S. Hauff, Instationäres thermodynamisches Verhalten einer alkalische Niedertemperatur-Brennstoffzelle, *VDI-Fortschr.-Ber., VDI Reihe 6, Nr. 293*, VDI, Düsseldorf, Germany, 1993.